High-throughput determination of Hubbard math xmlns="http://www.w3.org/1998/Math/MathML">mi>U/mi> /math> and Hund math xmlns="http://www.w3.org/1998/Math/MathML">mi>J/mi>/ math> values for transition metal oxides via the linear response formalism

Guy C. Moore, Matthew K. Horton, Edward Linscott, Alexander M. Ganose, Martin Siron, David D. O'Regan, and Kristin A. Persson

Phys. Rev. Materials **8**, 014409 — Published 29 January 2024

DOI: 10.1103/PhysRevMaterials.8.014409

High-throughput determination of Hubbard U and Hund J values for transition metal oxides via the linear response formalism

Guy C. Moore,[1,2] Matthew K. Horton,[1,2] Edward Linscott,[3] Alexander M. Ganose,[4] Martin Siron,[1,2] David D. O'Regan,[5] and Kristin A. Persson[1,6]

[1]*Department of Materials Science and Engineering, University of California Berkeley, Berkeley, CA 94720, USA*
[2]*Materials Science Division, Lawrence Berkeley National Laboratory, Berkeley, CA 94720, USA*
[3]*Theory and Simulations of Materials (THEOS), and National Centre for Computational Design and Discovery of Novel Materials (MARVEL), École Polytechnique Fédérale de Lausanne, 1015 Lausanne, Switzerland*
[4]*Energy Technologies Area, Lawrence Berkeley National Laboratory, Berkeley, CA 94720, USA*
[5]*School of Physics, SFI AMBER Centre and CRANN Institute, Trinity College Dublin, The University of Dublin, Ireland*
[6]*Molecular Foundry, Lawrence Berkeley National Laboratory, Berkeley, CA 94720, USA*

(Dated: October 13, 2023)

DFT+U provides a convenient, cost-effective correction for the self-interaction error (SIE) that arises when describing correlated electronic states using conventional approximate density functional theory (DFT). The success of a DFT+U($+J$) calculation hinges on the accurate determination of its Hubbard U and Hund J parameters, and the linear response (LR) methodology has proven to be computationally effective and accurate for calculating these parameters. This study provides a high-throughput computational analysis of the U and J values for transition metal d-electron states in a representative set of over 1000 magnetic transition metal oxides (TMOs), providing a frame of reference for researchers who use DFT+U to study transition metal oxides. In order to perform this high-throughput study, an `atomate` workflow is developed for calculating U and J values automatically on massively parallel supercomputing architectures. To demonstrate an application of this workflow, the spin-canting magnetic structure and unit cell parameters of the multiferroic olivine $LiNiPO_4$ are calculated using the computed Hubbard U and Hund J values for Ni-d and O-p states, and are compared with experiment. Both the Ni-d U and J corrections have a strong effect on the Ni-moment canting angle. Additionally, including a O-p U value results in a significantly improved agreement between the computed lattice parameters and experiment.

I. INTRODUCTION

Density functional theory (DFT) is a workhorse of computational materials science. However, the proper treatment of electronic exchange and correlation within the framework of DFT is a long-standing challenge [1]. Local density approximation (LDA) and generalized gradient (GGA) [2] functionals were developed to add exchange-correlation (XC) contributions to the energy functional within the Kohn–Sham (KS) formalism [3]. However, numerous studies have shown that these XC functionals have an associated self-interaction error (SIE) [1, 4, 5]. This shortcoming ultimately derives from the difficulty in quantifying exact exchange and correlation effects, without solving the many-body Schrödinger equation, using only density-based approximations.

Over the past couple of decades, DFT+U has found favor as a method that strikes a reasonable balance between accuracy and computational cost, making it particularly suitable for high-throughput computation [6–10]. DFT+U functionals add a correction to the conventional XC functional to account for the Coulombic interaction between localized electrons [4, 11]. In more recent studies, various researchers have explored extensions of DFT+U with the goal of further correcting for static correlation effects and delocalization errors [12–14].

One drawback to DFT+U type functionals is that one must first determine its associated parameters, the Hubbard U and Hund J, and possibly also inter-site electronic interactions denoted as "+V" [15–17]. The results of a DFT+U calculation can quantitatively and even qualitatively change depending on these parameters, and so obtaining reliable values is of paramount importance. This is as true for the Hund J as it is for the Hubbard U, even in the simplified rotationally invariant DFT+U_{eff} functional [18]. In this particular functional, the Hubbard U and Hund J are grouped in single effective Hubbard parameter U_{eff}, defined as $U_{\text{eff}} = U - J$. This formalism assumes spherically symmetric on-site interactions, and results in a corrective term that only couples electrons of the same spin [10, 18, 19]. Nevertheless, the reduction in the effective parameter by J can be significant.

While the aforementioned approximation may seem more justifiable for systems with no magnetic order, in the case of magnetic systems it results in a lost opportunity to use the Hund J to beneficially enhance the spin moments in simulated broken-symmetry ground states. Moreover, when we move to non-collinear magnetism, the spin texture of materials is particularly sensitive to screening interactions between spin channels [19–21]. In fact, magnetic exchange constants can be derived from

the extended Hubbard model, from which it is possible to relate exchange constants to ratios between U and J values [22]. The famous Hubbard model provides a simplified framework on which to explain the rich physics of correlated transition metal compounds [22]. Additionally, it has been shown that the Hund J term is important for describing important physical phenomena, such as Jahn-Teller distortions [22, 23], emergent intra-atomic exchange, and the Kondo effect [24, 25]. Therefore, the introduction of explicit unlike-spin exchange corrections beyond simplified rotationally invariant DFT+U_{eff} is clearly of interest, and this requires the treatment of the Hund J on the same footing as the Hubbard U.

A. Strategies for determining Hubbard parameters

A common approach for determining Hubbard U values is to tune them such that some desired result — for example, the DFT+U_{eff} band gap, or a formation energy — matches its experimental value, or a value obtained via more accurate and computationally expensive beyond-DFT methods [26, 27]. There are several problems with this strategy. Firstly, it is not systematic: just because one result (e.g., the band gap) now matches experiment, this does not guarantee the same will be true for other observables (e.g., local magnetic moments). Indeed, there are a multitude of reasons why DFT may not match experiment, and it is wrong to rely on Hubbard corrections to correct for errors that do not arise from self-interaction [28]. Secondly, this strategy is not predictive: it relies on the existence of experimental/beyond-DFT data. This makes it particularly ill-suited to the prediction of novel materials and high-throughput studies.

Yet another difficulty that arises is the lack of transferability of Hubbard and Hund parameters. It has been repeatedly shown that these parameters are in fact very sensitive to the local chemical environment [29]. Even the specific pseudopotentials [5] or the specific site occupation projection scheme [30] have a significant effect on the computed Hubbard U values. The end result is that U values (and by extension Hund J values, which are albeit normally less environment-sensitive) are not transferable: they cannot be tabulated, and must always be determined on a case-by-case basis.

These issues can be overcome by calculating the Hubbard and Hund parameters from first principles. The two primary methods for doing so are the constrained random phase approximation (cRPA) [31, 32] and the linear response (LR) methods [4, 10]. In this study, we focus on the LR method due to its lower computational cost compared to existing cRPA methods, which are not yet appropriate for high-throughput applications.

The linear response method, as introduced by Cococcioni and coworkers [4], is founded on the idea that SIE can be related to the behaviour of the total energy as a function of the total occupation [33]. It is known that the total energy ought to be piece-wise linear with respect to total site occupation numbers in the dissociated limit [34], but in fact for semi-local DFT XC functionals, the energy is erroneously convex at fractional electron numbers. Cococcioni and co-workers illustrated that the $+U$ correction counteracts this erroneous curvature within local subspaces (the hope being that correcting local curvature will help address the erroneous global curvature [35]). Crucially, the magnitude of this curvature can be directly measured by a DFT linear response calculation, allowing the value of U to be determined accordingly. Unlike empirical fitting, this approach is (a) systematic, because the value of U is derived directly as a measure of the underlying SIE present in the DFT calculation, and (b) it is predictive, because it only requires DFT calculations to extract the Hubbard parameters, and not experimental or beyond-DFT results.

B. Paper outline

The Materials Project is a web-based database that contains computed information on a vast range of materials, both experimentally established and computationally predicted [36]. Among the various computational results it presents are Hubbard parameters U_{eff}. However, these current default U_{eff} values were obtained by fitting DFT+U_{eff} energies to experimental formation energies for a selected number of redox reactions [29, 37]. This paper aims to replace these values with ones computed using linear response. In order to achieve this, we present a unified framework for computing on-site Hubbard and Hund corrections in a fully parallelized and automated computational workflow (which will be introduced in Section II). Using this workflow, we performed a high-throughput calculation of U and J values for a set of over one thousand transition-metal-containing compounds. This provides us with a novel, big-picture point-of-reference for the sensitivity of U and J across a wide range of systems of varying chemistries and local chemical environments (Sections III A and III B). A subset of the values presented in Section III A are hosted publicly at Ref. 38. We then explore the effects of these Hubbard corrections on magnetic materials that exhibit a rich variety of non-collinear spin configurations, exemplified through the spin canting structure of olivine $LiNiPO_4$ (Section III C).

II. METHODS

A. The Hubbard functional

The Hubbard functional is a corrective functional, in the sense that it involves adding a corrective term $E_{\text{Hub}} - E_{\text{dc}}$ on top of some base functional E_{DFT} (typically a local or semi-local functional), resulting in a total energy

functional

$$\begin{aligned} E_{\mathrm{DFT}+U+J}&\left[\rho,\left\{\boldsymbol{n}_\gamma^\sigma\right\}\right] \\ &= E_{\mathrm{DFT}}\left[\rho\right] \\ &\quad + E_{\mathrm{Hub}}\left[\left\{\boldsymbol{n}_\gamma^\sigma\right\}\right] - E_{\mathrm{dc}}\left[\left\{n_\gamma^\sigma\right\}\right] \\ &= E_{\mathrm{DFT}}\left[\rho\right] + E_{U/J}\left[\left\{\boldsymbol{n}_\gamma^\sigma\right\}\right] \end{aligned} \tag{1}$$

The $(\boldsymbol{n}_\gamma^\sigma)_{mm'} = \langle\varphi_{\gamma m}|\hat{\rho}^\sigma|\varphi_{\gamma m'}\rangle$ are matrices that represent the projection of the (spin-dependent) density operator onto Hubbard subspaces (indexed γ) defined by some set of orbitals $|\varphi_{\gamma m}\rangle$. These orbitals are typically atom-centred, fixed, spin-independent, localised, and orthonormal, often corresponding to the $3d$ or $4f$ subshell of a transition metal or lanthanide. The n_γ^σ occupation numbers are the corresponding traces of $\boldsymbol{n}_\gamma^\sigma$ matrices.

In the following paragraphs, we will provide a summary of some of the most well known formulations of DFT+U(+J). We note that because we are interested in the fully localized limit (FLL), we will not discuss extensions of DFT+U+J to metallic systems, where an "around mean field" (AFM) double-counting correction may be more appropriate [10].

Starting from DFT+U+J implementations of the highest complexity, and moving forward through increasing levels of simplification, we introduce the rotationally invariant implementation proposed by Liechtenstein et al. [39]. Within this flavor of DFT+U+J, E_{Hub} and E_{dc} take the following form

$$\begin{aligned} E_{\mathrm{Hub}} = &\frac{1}{2}\sum_{\{m\},\gamma,\sigma}\langle m,m''|V_{ee}|m',m'''\rangle(n_\gamma^\sigma)_{mm'}(n_\gamma^{-\sigma})_{m''m'''} \\ &+\frac{1}{2}\sum_{\{m\},\gamma,\sigma}\left\{\langle m,m''|V_{ee}|m',m'''\rangle - \langle m,m''|V_{ee}|m''',m'\rangle\right\}(n_\gamma^\sigma)_{mm'}(n_\gamma^\sigma)_{m''m'''} \end{aligned} \tag{2}$$

$$E_{\mathrm{dc}} = \sum_\gamma \frac{U_\gamma}{2} n_\gamma\left(n_\gamma - 1\right) + \sum_{\gamma,\sigma}\frac{J_\gamma}{2} n_\gamma^\sigma\left(n_\gamma^\sigma - 1\right), \tag{3}$$

where $\langle\cdot|V_{ee}|\cdot\rangle$ are the Coulomb integrals projected on the orbital basis, indicated by the associated $\{m\}$ set of quantum numbers [10, 12, 39]. This correction is parameterized by both Hubbard U_γ and Hund J_γ coupling constants through the double-counting energy contribution, E_{dc}.

As an aside, we note that it is possible to extend this formalism to non-collinear magnetism, which is essential for the inclusion of spin-orbit coupling (SOC). In this case the on-site occupation matrix acquires off-diagonal elements $(n_\gamma^{\sigma,\sigma'})_{mm'}$, in accordance with the spinor extension of DFT, and DFT+U+J by extension [19–21, 40]. Within this formalism, the notion of "up" and "down" spin electron densities is tied to the eigenvalues of the $n^{\sigma,\sigma'}$, and become $n^\uparrow = \frac{1}{2}\left(n + |\boldsymbol{m}|\right)$ and $n^\downarrow = \frac{1}{2}\left(n - |\boldsymbol{m}|\right)$, where $\boldsymbol{m} = [m_x\ m_y\ m_z]^T$ is the magnetization, on-site or otherwise [41]. Equations 2 and 3 still apply to the non-collinear case, provided $(n_\gamma^\sigma)_{mm'}$ are obtained from a spin-diagonalization of $(n_\gamma^{\sigma,\sigma'})_{mm'}$.

Simplified versions of Equations 2 & 3 were proposed by Dudarev et al. [18], and later by Himmetoglu and coworkers [42], which approximate $\langle\cdot|V_{ee}|\cdot\rangle$ using Slater integrals, which can be parameterized through U and J values. There are many helpful explanations for this approximation, such as those summarized in Refs. 10 and 12.

In the spirit of following increasing levels of simplification, we will start with the Himmetoglu implementation [42], inspired by the work of Solovyev et al. [43]. Using the Slater integral parameterization of U and J, it is possible to approximate and simplify $E_{U/J}$ from Equations 2 & 3 into the following

$$\begin{aligned} E_{U/J} = E_{\mathrm{Hub}} - E_{\mathrm{dc}} = \\ \sum_{\gamma\sigma}\frac{U_\gamma - J_\gamma}{2}\mathrm{Tr}\left[\boldsymbol{n}_\gamma^\sigma(1-\boldsymbol{n}_\gamma^\sigma)\right] + \sum_{\gamma\sigma}\frac{J_\gamma}{2}\mathrm{Tr}\left[\boldsymbol{n}_\gamma^\sigma\boldsymbol{n}_\gamma^{-\sigma}\right]. \end{aligned} \tag{4}$$

A well known further simplification of Equation 4, notwithstanding that it substantially pre-dated the latter, is the formulation of DFT+U_{eff} put forth by Dudarev et al. [18] and given by

$$E_U = E_{\mathrm{Hub}} - E_{\mathrm{dc}} = \sum_{\gamma\sigma}\frac{U_\gamma^{\mathrm{eff}}}{2}\mathrm{Tr}\left[\boldsymbol{n}_\gamma^\sigma(1-\boldsymbol{n}_\gamma^\sigma)\right]. \tag{5}$$

As discussed in the Introduction, this approximation arises by assuming spherical symmetry of the Coulomb interactions, $\langle\cdot|V_{ee}|\cdot\rangle$ [10, 12, 42]. Within the simplified Dudarev DFT+U_{eff} of Equation 5, the effective Hubbard U becomes $U_\gamma^{\mathrm{eff}} = U_\gamma - J_\gamma$ [10, 12, 18].

B. Hubbard U and Hund J spin polarized linear response

The DFT+U_{eff} correction of Equation 5 adds a convex energy penalty to fractional occupations of the orbitals that diagonalize $\mathbf{n}_\gamma^\sigma$, which can (in principle) counterbalance the SIE present in these Hubbard subspaces. In the linear-response approach, one measures the curvature in the total energy as a function of the subspace occupancy, and then chooses a value U to match the observed curvature. Naïvely computing this energy curvature as a function of the subspace occupancy would require a constrained DFT calculation, but one can recast the problem and instead measure the energy curvature with respect to the magnitude v_γ of an on-site perturbing potential $\hat{v}_\gamma = \sum_{mm'} v_\gamma |\varphi_{\gamma m}\rangle\langle\varphi_{\gamma m'}|$. The energy functional is then given by

$$E[\{v_\gamma\}] = \min_{\rho(\boldsymbol{r})} \left\{ E[\rho(\boldsymbol{r})] + \sum_\gamma v_\gamma n_\gamma \right\} \tag{6}$$

from which one computes the response matrices

$$\chi_{\gamma\gamma'} = \frac{\partial n_\gamma}{\partial v_{\gamma'}}. \tag{7}$$

Thus far we have used a general index "γ" to represent each site. Conventionally, this index refers purely to the atom γ on which the Hubbard site is centered. In this case, the Hubbard parameter for that subspace is given by

$$U_\gamma = \left(\chi_0^{-1} - \chi^{-1}\right)_{\gamma\gamma} \tag{8}$$

where χ and χ_0 are the interacting, (or self-consistent) and non-interacting (or non-self consistent) response matrices [4, 10]. We note that the sign of the response matrices in Equation 8 is consistent with the foundational linear response body of literature, such as in Ref. 4, however, they are defined as having opposite sign within VASP (Vienna ab initio Simulation Package) [44].

The above strategy does not delineate between spin channels: during the linear-response calculations the spin-up and spin-down channels are perturbed simultaneously by the same amount, i.e., $v_\gamma^\uparrow = v_\gamma^\downarrow$ and we only observe the change in total occupancy $n_\gamma = n_\gamma^\uparrow + n_\gamma^\downarrow$. If we want to calculate J, one must instead consider the spin-dependent perturbation

$$\hat{v}_\gamma^\sigma = \begin{cases} +\sum_{mm'} v_\gamma |\varphi_{\gamma m}\rangle\langle\varphi_{\gamma m'}| & \sigma = \uparrow \\ -\sum_{mm'} v_\gamma |\varphi_{\gamma m}\rangle\langle\varphi_{\gamma m'}| & \sigma = \downarrow \end{cases} \tag{9}$$

and then construct a second set of response matrices which then relate to J in a completely parallel approach [45] to the calculation of U in Equation 8.

A separate but ultimately equivalent strategy is to treat the spin channels separately [5]. In this case a general index runs over both the atom index $\gamma = \{1, ..., N\}$ and also the two spin channels $\sigma = \{\uparrow, \downarrow\}$. In this case the response matrices of Equation 7 become rank-four tensors, i.e.,

$$\chi_{\gamma\gamma'}^{\sigma\sigma'} = \frac{\partial n_\gamma^\sigma}{\partial v_{\gamma'}^{\sigma'}}. \tag{10}$$

and now the equivalent of Equation 8 is

$$f_{\gamma\gamma}^{\sigma\sigma'} = \left(\chi_0^{-1} - \chi^{-1}\right)_{\gamma\gamma}^{\sigma\sigma'} \tag{11}$$

where now we must now prescribe how to map the 2×2 matrix $f_{\gamma\gamma}^{\sigma\sigma'}$ to the scalar parameters $U_\gamma = G_U(f_{\gamma\gamma}^{\sigma\sigma'})$ and $J_\gamma = G_J(f_{\gamma\gamma}^{\sigma\sigma'})$. Possible definitions for these mappings G_U and G_J are motivated and explored in detail in Ref. 5, but the end result is the following: there are two possible approaches. In the first approach one can define this mapping in order to recover the U_γ and J_γ that one would obtain using the conventional spin-agnostic approach of Equations 8 and 9. In this approach, the spin moment is permitted to vary during a charge perturbation, and vice versa. We will hereafter refer to this as the "conventional" strategy (in the language of Ref. 5 this is the "scaled" approach). Throughout this work, unless otherwise stated, we will use the conventional strategy, which as the name suggests is the one that has been in almost universal use to date.

In the second approach, one defines the mapping to impose the condition that the local magnetic moment (local occupation) is held fixed during the perturbation while calculating the Hubbard (Hund) parameter, specifically by means of the the equations rather than in the explicit sense of fixing these quantities using constrained DFT. We will refer to this as the "constrained" approach (the "simple" approach in Ref. 5). This approach has recently been demonstrated to be the correct one for use with a DFT+U type functional "BLOR" explicitly designed to impose the flat-plane condition upon subspaces [34]. The spin-polarized linear response formalism permits us to compute the "constrained" approach U and J values simultaneously, at no additional cost.

C. Implementation of linear response within a high-throughput workflow

The linear response method was implemented as a workflow within the high-throughput `atomate` framework [46]. The workflow allows the user to compute Hubbard U and Hund J values using either a spin-polarized or a non-spin-polarized response. In addition to screening between spin channels, the implementation provides the straightforward extension to multiple levels of screening, including inter-site and inter-spin-channel responses [5]. A more detailed explanation of how these screening ma-

trices are computed is provided in Appendix A.

All of the individual calculations within this workflow were performed with VASP (Vienna ab initio Simulation Package) [44], a plane-wave DFT code. The PBE exchange-correlation functional was used throughout as the base functional [47]. Unless otherwise stated we use PAW PBE pseudopotentials, which are the default pseudopotentials for the `pymatgen` input sets for VASP [48]. In this regard, our work supplements the high-throughput work of Bennett et al. [49] where ultrasoft pseudopotentials were used to reduce computational cost in high-throughput computations [49], mirroring early foundational studies on the linear response method [4, 15].

We have used an automatic k-point generation scheme that uses 50 k-points per reciprocal angstrom, and a cutoff energy of 520 eV. The full set of input parameters can be found in the `HubbardHundLinRespSet` in the `atomate` repository [50], and the derived VASP input sets in the `pymatgen` repository [48]. For the linear response analysis, the on-site applied potential $v_{I\sigma}$ range was from -0.2 eV to $+0.2$ eV (-0.05 eV to $+0.05$ eV for the periodic table data set) sampled at nine points at uniform intervals. In Appendix C, we address the sensitivity of the linear response analysis to the truncated precision in VASP's occupation number I/O, which we observed for some TMO systems.

III. RESULTS

Hubbard U and Hund J values were calculated for over one thousand transition metal oxides using the linear response workflow implemented in `atomate`. The majority of the calculations corresponded to materials containing Mn-d, Fe-d, and/or Ni-d species. All the systems studied were previously predicted by Ref. 51 to have a collinear magnetic ground-state using a separate high-throughput workflow. That work used the empirical Hubbard U values reported on the Materials Project.

In addition, a representative set of O-p responses were calculated and analyzed. It is less common to include Hubbard corrections to oxygen $2p$ states. However, an appreciable number of studies have shown how O-p on-site corrections have improved the agreement with experimentally measured bond lengths between oxygen and transition metal species [5, 45, 52–55]. It is perhaps less intuitive to apply spin-polarized Hund J parameters to oxygen sites, because O-p states are conventionally not included in effective models for magnetism. However, while oxygen atoms do not develop magnetic moments, early studies have demonstrated theoretically and computationally that O-p states mediate the antiferromagnetic superexchange interaction in transition metal oxides, such as MnO [22, 56, 57].

TABLE I: Comparison of computed U_{eff} in the present work with values used by the Materials Project [29, 37].

element	mean U_{eff} (eV)	$U_{\text{eff}}^{\text{MP}}$ (eV)	diff. (eV)
Co	4.430 ± 1.474	3.32	1.110
Cr	2.425 ± 0.472	3.7	-1.275
Fe	4.108 ± 1.322	5.3	-1.192
Mn	4.135 ± 0.724	3.9	0.235
Mo	1.911 ± 0.318	4.38	-2.469
Ni	5.258 ± 0.773	6.2	-0.942
V	3.060 ± 0.673	3.25	-0.190
W	1.461 ± 0.218	6.2	-4.739

A. Periodic table sample set

Figure 1 displays two periodic tables containing the distributions of computed Hubbard U_{eff} and Hund J values for each transition metal element (and oxygen) computed for different structures within the database. In Table I, values obtained in this study are listed alongside the standard U_{eff} values employed by the Materials Project [29, 37]. Those values were determined using the procedure outlined by Wang et al. [59] which finds a U_{eff} value that minimizes the error in formation energy for several representative redox couples. Due to the limited amount of experimental data available, these U_{eff} values are determined with only experimental data from a single redox couple (Co, Cr, Mo, Ni, and W) or two redox couples (Fe, Mn, and V). Therefore, it is possible or likely that these U_{eff} values are not appropriate for a more general system containing these elements. Nevertheless, the MP U_{eff} values are found to be the same as the U_{eff} values in the present work within the standard deviation for most elements (Co, Fe, Mn, and V) or slightly outside the value in the present work (Ni). Exceptions are Cr, Mo, and W, with the largest, notable discrepancy of 4.739 eV for W.

To evaluate the impact of these discrepancies, compounds containing W from a dataset of experimental formation energies [60] used by the Materials Project were taken and relaxed using the new U_{eff} value for W from the present work but with all other calculation settings kept consistent with standard Materials Project settings, to obtain a new set of computed energies. These energies substantially lowered the correction introduced in Ref. 60 for W from -4.437 eV/atom to 0.12 eV/atom, suggesting that the newer U_{eff} is indeed more appropriate for the calculation of formation energies.

We stress that these values are not transferable to studies that use DFT+U+J implementations in other codes. Quantum ESPRESSO and Abinit use localized projections that are separately different from that in the projector augmented wave (PAW) method implemented in VASP [30], for different reasons.

The trends across these periodic tables — and in particular, the increasing U across the $3d$ transition met-

(a) Periodic Table of Hubbard U values computed from first principles.

(b) Periodic Table of Hund J values computed from first principles.

FIG. 1: Periodic table of Hubbard U and Hund J values computed for representative set of transition metal oxides. The color map indicates the mean value computed for each element over each material. The materials used in the creation of these periodic tabled were selectively chosen: noting that many databases, including the ICSD, contain a growing number of hypothetical materials which may or may not be realizable, we selected materials that are well-studied and exhibit more than two ICSD IDs each. Furthermore, to remove cross-correlations between magnetic elements, we also require that these compounds only contain a single d-block element (occupying a single symmetrically-equivalent site) with no f-block species. Ultimately, these data correspond to the U and J values for over 800 materials, and are distributed over the transition metal species. A more detailed table containing data on the distribution of values is included in Table V in the Appendix. The plotted distributions of U/J values are generated using a Gaussian kernel-density estimator implemented in `scipy` [58].

als — are reminiscent of results from early studies that related the Hubbard and Hund parameters to Slater integrals over the Coulomb operator [10, 18, 61, 62]. For example, Ref. [61] proposes a linear relationship between the atomic number Z and the Hubbard and Hund parameters, based on both Hartree-Fock calculations and empirical observations. Note, however, that this is only valid for unscreened Coulomb kernels [10], and the Slater integrals are in fact highly dependent on the screening of Coulomb exchange between electrons (and hence the chemical environment) [10, 32]. We also do not want to overstate this comparison, which mixes older definitions of the Hubbard and Hund parameters (i.e. as derived from Slater integrals) with those used in this work (i.e. as measures of the deviation of the DFT functional from piecewise linearity).

B. Focused study on Mn-d, Fe-d, Ni-d, and O-p, including the reason for large O-p Hubbard U values

We now present a more detailed study on materials containing Mn-d, Fe-d, Ni-d, and O-p Hubbard sites. For these systems, the distributions of the computed Hubbard U and Hund J values are provided in Figure 2. The variations in U and J values calculated for these three species is immediately apparent, with a range on the order of approximately 1 to 2 eV. These distributions reflect the intrinsic screening environment dependence of the calculated value for a given element. At this point, we note only their apparently universal unimodality (single peak) and the near-general decrease in U with chemical period within a given group, however we will return presently to a more physically and chemically motivated observation. In Table II we list for comparison the U values currently used in Materials project (fitted empirically) as well as a range of U values found for a set of spinels and olivines by Zhou and co-workers (calculated via self-consistent linear response) [29].

We find that O-p exhibits the largest associated Hubbard U value of approximately 10 eV, which agrees with the linear response results from a previous study using a different code and somewhat different linear-response formalism [5]. While large oxygen Hubbard U values may seem surprising within a strongly correlated materials context, it has become more accepted in recent years within first-principles solid-state chemistry that oxygen $2p$ orbitals can warrant, both by direct calculation and by necessity (when resorting to fitting), a remarkably high U value in DFT+U.

1. *Interpretation of Hubbard U in terms of the subspace chemical hardness*

We will now attempt to motivate and explain the phenomenon of comparatively larger O-p U values. We note from the outset that the element projector orbital profile plays a complicating role in the following analysis. Over a sample of materials, we observe that the 2×2 averaged diagonal elements of the χ_0^{-1} non-interacting response are of approximately the same magnitude for both TM-d and O-p site matrix elements, with a mean difference close to zero. The non-self-consistent response can be interpreted as the response due to non-interacting response effects at a site due to its surroundings [10], and thus it can be understood as a property primarily of the environment of the atom under scrutiny. Then, unless screening is very short ranged (as it may be in a very wide-gap insulator), this quantity may be said to be somewhat similar, on average, for metal and oxygen ions in an oxide. Thereby, the chemical trends in the Hubbard U arise mostly in the interacting response, instead.

Next, for this same sample of materials, we note that the magnitude of the O-p interacting response χ tends to be significantly less than the interacting TM-d response. This indicates that $-\chi^{-1} = d^2E/dn_\gamma^2$, the curvature of the total energy versus occupation, n_γ, is greater for O-p states. This greater curvature versus occupation can be explained in terms of known trends in the chemical hardness, i.e., the second chemical potential, i.e., the derivative of the chemical potential with respect to total charge at fixed external potential. (We note in passing that some authors choose to include a factor of one half in the definition of the chemical hardness for historical reasons, but we suppress that discussion here.) Specifically, we can focus on the finite difference (three-point) approximation to the global chemical hardness [63], namely

$$\begin{aligned}\nu &\equiv d^2E/dN^2 \approx E\left(N-1\right) - 2E\left(N\right) + E\left(N+1\right) \\ &= \left[E\left(N+1\right) - E\left(N\right)\right] - \left[E\left(N\right) - E\left(N-1\right)\right] \\ &\equiv E_i - E_a \equiv E_g, \end{aligned} \tag{12}$$

which is nothing but the fundamental band-gap. This is a quantity that has been tabulated many times. Using the results of Ref. 64, we find that for atomic oxygen its value is 11.2 eV, compared to that of the transition metal atoms, where it ranges from 5.8 eV (Ti & Zr) to 8.0 eV (Mn) if we exclude the often problematic zinc group, where it reaches 11.6 eV. This mirrors and explains the observed relatively large first-principles Hubbard U value for oxygen $2p$ states predicted in this and several previous studies.

Ultimately, we conclude that the Hubbard U may be interpreted as the subspace-projected, environment-screened chemical hardness. More precisely, U can be intuited as contributions to the hardness due to interactions such as Hartree, exchange, correlation, and perhaps other terms like implicit solvent and PAW potential. After all, it is from these interactions that most chemical trends appear to arise in practice. For subspaces that project heavily at both band-edges, as in normal DFT+U_{eff} practice, the U inherits chemical trends from the chemical hardness (fundamental gap) of the atom that it resides upon. This is higher for a greater atomic ionization energy E_i (that of oxygen is generally around

TABLE II: Computed range of U, J, and U_{eff} values compared with reported U_{eff} on the Materials Project (MP) [37], as well as the MP literature [29]. Each mean value has an associated standard deviation indicated after the "±."

Species	mean computed U (eV)	mean computed J (eV)	mean computed $U_{\text{eff}} = U - J$ (eV)	reported MP [37] U_{eff} (eV)	reported range [29] U_{eff} (eV)
Mn-d	4.953 ± 0.635	0.520 ± 0.156	4.433 ± 0.654	3.9	3.60 – 5.09
Fe-d	4.936 ± 0.700	0.177 ± 0.367	4.759 ± 0.790	5.3	3.71 – 4.90
Ni-d	5.622 ± 1.221	0.399 ± 0.434	5.223 ± 1.296	6.2	5.10 – 6.93
O-p	10.241 ± 0.910	1.447 ± 0.171	8.794 ± 0.926	N/A	N/A

twice that of transition metals) and higher also for a more negative electron affinity E_a (that of oxygen is more negative than that of most but not all transition metals). By and large, both quantities are well known to increase in magnitude as we move 'up and right' in the periodic table, and this same broad trend is reflected in our periodic table of Hubbard U values.

When a DFT+U_{eff} subspace projects only onto one band edge, as is the case for charge-tranfer insulators, then only the trend in either the ionization energy or electron affinity will be very relevant to the trends in U. Due to the relatively large electronegativity of oxygen, typically there will be little weight at the conduction band edge for oxygen $2p$ orbitals projectors. Therefore, the particularly clear trend in ionization energy drives the relatively large U value for oxygen. Indeed, if this argument holds, then one would guess that the oxygen $2p$ U value is roughly twice that of an average transition-metal d-subspace, which turns out to be the case from first principles linear response.

Within the present formalism, the Hund J may be interpreted as an analog for the spin degree of freedom, and specifically as minus (by a convention thought to originate with Ising) the interaction part of the subspace-projected, environment screened spin-hardness, where the spin-hardness is a quantity discussed for example in Ref. 65.

2. *Trends in U and J values*

In order to explore trends in the distribution of U and J values, we have plotted these on-site corrections in scatter plots within Figure 2. These plots illustrate the relationship between U and J values with respect to site occupations. For transition metal species, we plot U and J versus the "d" component of the projected moment m, denoted as "$m_{l=2}$." These moment values are those output by VASP as the difference between up and down spin site occupancy numbers computed using PAW core-region operators. Because the oxygen atoms do not have an associated magnetic moment, we plot O-p Hubbard U and Hund J versus $n_{l=1}$ occupations on oxygen sites.

We should stress that the values of "m_l" and "n_l" are only computed from the calculation without the $+U/J$ correction. One reason for using the bare PBE computed m_l and n_l is that these occupations should be independent from the applied Hubbard U or Hund J values. This would offer the "bare" m, as well as n, as a possible predictors of U and J values. However, it is important to note that these occupations could change significantly with applied U and J values [5, 66, 67].

There is an apparent clustering of datapoints at different on-site m_l magnetizations in Figures 2a, 2b, and 2c. This grouping at different on-site magnetization values is most likely due to different spin and charge states dependent on the underlying chemistry. We also observe a larger range of U and J values for higher values of m_l, which is due to the coupling between highly spin-polarized states to on-site Coulomb screening for TM species. As would be expected, we see similar trends for J, a measure of the screened interaction between spin channels.

The clusters that lie at the associated maximum computed m_l fall off and exhibit a negative slope trend with the magnitude of the site moment. This is likely due to the fact that m_l is highly dependent on the local chemical environment, which will govern the interacting and non-interacting energy curvatures with respect to spin-occupations, which are related to U and J within linear response [4]. The clear trend for the manganese may be due to the strong tri-modal distribution of Mn magnetic moments seen in Figure 1 of Ref. 51. The "stable" magnetic configurations from this study were used in the LR analysis, therefore a similar statistical distribution should hold for the subset of structures used in this LR analysis.

The trends of the datapoints for Hubbard U and Hund J values in Figure 2d appear to show a downward trend for U versus p-occupation numbers, $n_{l=1}$, and a slower, upward trend for J values versus $n_{l=1}$. We expect that the $n_{l=1}$ occupations will be strongly dependent on the oxidation/reduction state of oxygen atoms. Due to the nature of TM-O bonding in these oxides, and their generally greater electronegativity, the oxygen atoms will tend to maximize their valence. Therefore, building on the previous explanation of the magnitude of O-p U values based on chemical hardness and specifically the more relevant ionization potential component of that, the higher electron count for oxygen corresponds to a lower ionization potential, and therefore to a reduced Hubbard U, as

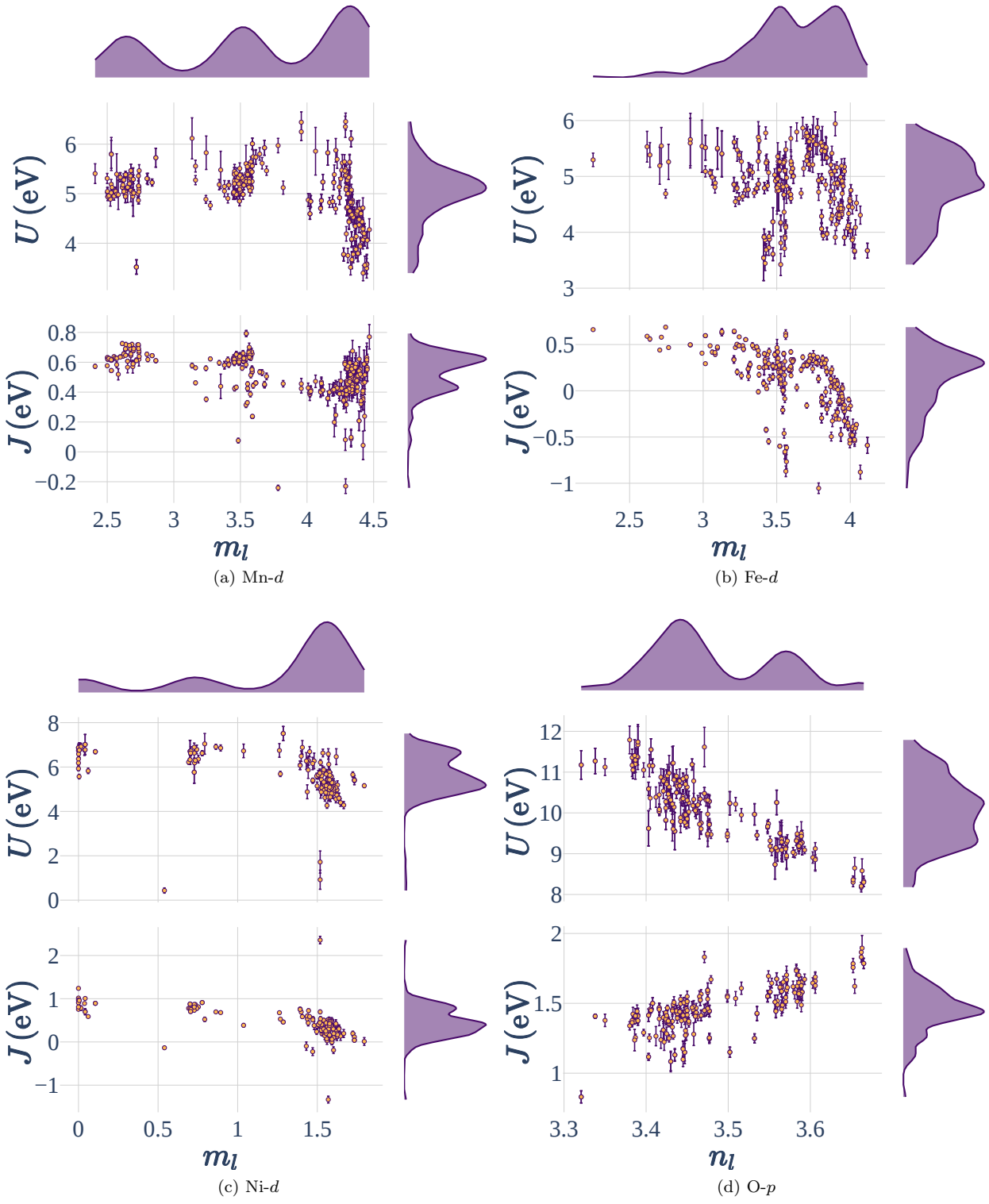

(a) Mn-d (b) Fe-d

(c) Ni-d (d) O-p

FIG. 2: Distributions of Hubbard U and Hund J values computed using the linear response method; For the sub-figures (a), (b), and (c) that correspond to d-electron TM site corrections, the U and J values are plotted against the DFT (no $+U+J$ correction) computed site magnetic m_l, where $m_{l=2}$ corresponds to the d-character of the local moment, which has an $l = 2$ angular momentum quantum number. The O-p U and J values in sub-figure (d) are plotted against n_l (the p-occupation in the case of O-2p) total site occupations. The number of samples for on-site correction values for Mn-d, Fe-d, Ni-d, and O-p are 285, 248, 149, and 206, respectively.

observed.

3. *Exploration using random forest regression*

To more robustly tease apart these observed trends, we performed a rudimentary random forest regression test on the dataset, ultimately in an attempt to predict the on-site corrections U and J from the input crystal structures and site properties. We used the random forest regression algorithm as implemented in `scikit-learn`. The input quantities supplied to the random forest regression routine consisted of the corresponding PBE-computed m_l and n_l (i.e. without on-site corrections), as well as the oxidation state estimated using the bond-valence method [68], and finally a selection of relevant site featurizers provided by the `matminer` Python package [69]. Unsurprisingly the U and J values appeared to be the most sensitive to the magnetic moment magnitude, $m = n_\uparrow - n_\downarrow$, and site occupation, $n = n_\uparrow + n_\downarrow$. This is in accordance with what would be expected from the dependence on the Hubbard U values on spin and charge state [66, 67]. However, these features proved to be insufficient to accurately predict U and J.

Most of the `matminer` site featurizers were tested as input to the random forest regression model. Additionally, the oxidation states calculated using the bond valence method (BVM) [68] were also included as input to the model. For learning trends across different atomic species, the atomic number of the associated element was also supplied. Additionally, we tested the orbital field matrix (OFM) features as formulated by [70, 71]. The OFM encodes the orbital character of the surrounding chemical environment. For more information on this method please refer to Ref. 70. The OFM functionality is not implemented in `matminer` or `pymatgen`. We were motivated to test the vectorized OFM by the chemical intuition that on-site Hubbard U and Hund J values are very sensitive to the local chemical environment. Additionally, the OFM has demonstrated success in predicting DFT-computed magnetic moments in the past [70]. Furthermore, the OFM nearest-neighbor contributions are weighted according to the geometry of the Voronoi cell, which could possibly provide information beyond the relative importance of the Voronoi `matminer` featurizer. Of the `matminer` featurizers, Ewald energy and Voronoi site featurizers had the greatest associated importance metric [69], second only to the on-site magnetization m_l. The on-site magnetization for Mn, Fe, and Ni, respectively, had an importance of at least ten percent more than any of the other local chemical environment descriptors.

From Hund's rules, it is possible to derive magnetochemistry rules governing the coupling between the magnetic spin-moment and associated charge state, dictated by the associated multiplet ground-state [61, 72, 73]. Therefore, the correlation between on-site corrections and projected site moments is not surprising. After all, previous studies have explored the connection between

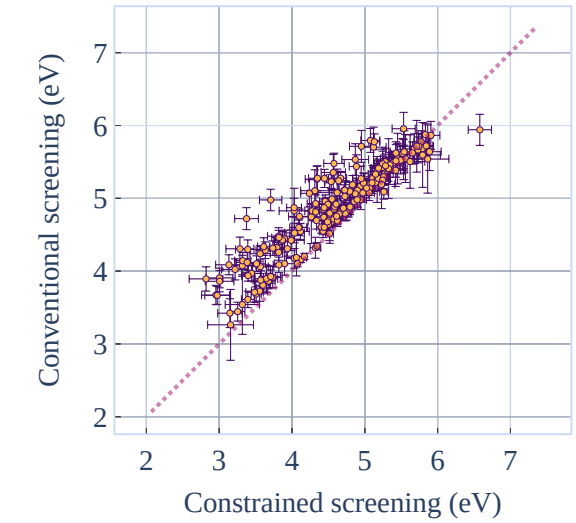

(a) Hubbard U (Fe-d)

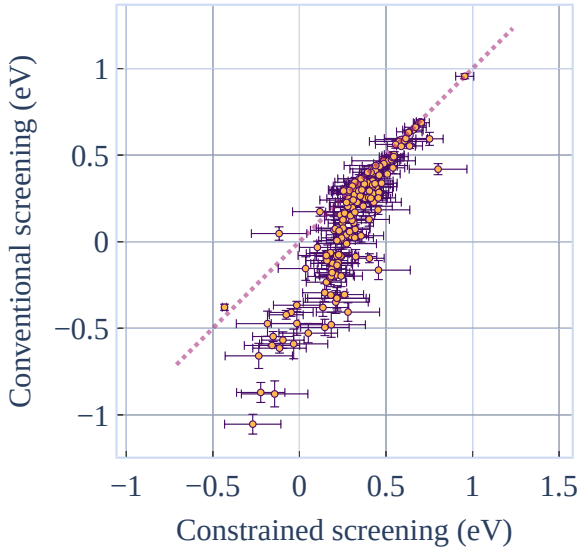

(b) Hund J (Fe-d)

FIG. 3: Comparison between the conventional and constrained approaches for calculating (a) Hubbard U and (b) Hund J values for Fe-d Hubbard sites.

charge states of transition metal species and the integrated net spin calculated from DFT [74–76]. In fact, recent studies show that the magnetic moment is often the most convenient and reliable indicator of charge states [74].

4. *Conventional vs. constrained linear response*

In introducing the linear response theory in Section II B, we mentioned that there are two possible schemes for computing U and J: "conventional" and "constrained" linear response, where in the latter case the

linear response is performed in such a way that the magnetic moment (occupation) is held fixed while measuring the curvature with respect to the occupation (magnetic moment). While arguments can be made as to theoretically which approach is the most valid for a given corrective functional (a topic which is the subject of ongoing research [34]), this dataset presents an opportunity to evaluate how much this choice will practically affect the resulting Hubbard and Hund parameters.

For the majority of the computed U and J values using these two methods, the difference between the two strategies fell within their computed uncertainty. However, we observed a significant deviation from $y = x$ behavior for the computed U and J values for iron Hubbard U and Hund J values shown in Figure 3. The width of this deviation from equality is greater than 1 eV for U in some regions, which is enough to affect computed physical properties [4, 66].

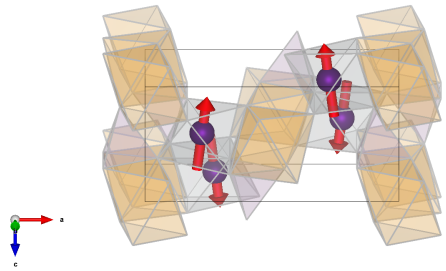

FIG. 4: Olivine crystal structure of $LiNiPO_4$ with magnetic atoms visible. Taken from [79] via the Bilbao MAGNDATA database [79, 80]. The purple atoms correspond to magnetic nickel atoms. The oxygen octahedra surrounding lithium atoms are indicated in orange, where the grey oxygen octahedra surround nickel sites.

5. *Dependence on structure and magnetic state*

For some input magnetic structures, the magnetic configuration changed while applying the on-site potentials during the linear response analysis. Our hypothesis is that the input magnetic structure corresponds to a local minimum configuration, or possibly a metastable state. Therefore, in our analysis, we screen out these structures with the intent that these systems will be studied in the future using a self-consistent approach to calculating on-site corrections.

In order to test the sensitivity of U and J values to the input structure specifically, we perform a geometry-self-consistent linear response study of antiferromagnetic NiO, which is provided in the Supplementary Information [77]. Each iteration consists of a step which includes geometry optimization of cell shape, followed by a linear response calculation of the PBE-based U and J values at the DFT+U+J geometry (so as to isolate the impact of the geometry from the matter of parameter self-consistency). These on-site correction values are then used in the next subsequent geometry optimization step. Self-consistency is achieved once the U and J values fall within their corresponding uncertainty values. Starting from the input structure — which was optimized using the current default Materials Project U values [37] — convergence was achieved after only two iterations.

It has been well established in previous studies that U values should be computed self-consistently with geometry optimization [66, 78]. As demonstrated from the experiments with antiferromagnetic NiO in the Supplementary Information [77], both the Hubbard U and Hund J values should be calculated self-consistently. In this self-consistency study, J had the largest relative convergence, and therefore appeared to be most susceptible to geometric self-consistency. Due to the coupling between Hund J and magnetic exchange [22], it is possible that both magnetic and structural features should be included in the self-consistency cycle. Within the `atomate` framework, it would be possible to incorporate an iterative workflow that wraps the workflow developed in this study, in order to alternate linear response calculations with geometry relaxation until self-consistency is achieved.

C. Case study: $LiNiPO_4$

We now present a detailed study on the olivine $LiNiPO_4$, designed to test the results produced by the linear response workflow. Previous GGA+U and GGA+U+J studies have attempted to reproduce the experimentally-observed spin-canting structure and unit cell shape as shown in Figure 4 [19, 29, 79].

We calculated U and J for this system via spin-polarized linear response. The spin-polarized linear response method introduced in Section II B can be generalized to non-collinear DFT using the relationship between spin-density occupations and the magnitude of the magnetic moment: $n_\uparrow = \frac{1}{2}\left(n + |\vec{m}|\right)$ and $n_\uparrow = \frac{1}{2}\left(n - |\vec{m}|\right)$ [21]. Within the context of linear response, this simplification is akin to assuming that E_{Hub} and E_{dc} can be stated as functionals of n and $|\vec{m}|$ alone. As we discussed in Section II A, this assumption is justified in both collinear and non-collinear (with spin-orbit coupling) DFT+U+J, as stated in Equations 2 and 3. Reassuringly, $|\vec{m}|$ and m hold similar meanings in both non-collinear and collinear DFT, respectively.

For comparison to the "non-collinear" results, we also performed a collinear calculation, where the magnetic configuration for $LiNiPO_4$ was obtained by projecting the canted non-collinear structure shown in Figure 4 along the z-direction. In addition to one unit cell of the the collinear antiferromangetic (AFM) configuration, a linear response analysis was performed on a 1×2×2 supercell. Table III summarizes the results of the computed Hubbard U and Hund J values. From this table, it is evident

TABLE III: Hubbard and Hund results for Ni-d in $LiNiPO_4$ (Atom-wise screening).

cell	magnetism	U (eV)	J (eV)
$1 \times 1 \times 1$	collinear	5.43 ± 0.16	0.38 ± 0.07
$1 \times 2 \times 2$	collinear	5.44 ± 0.24	0.54 ± 0.07
$1 \times 1 \times 1$	non-collinear	5.09 ± 0.15	0.42 ± 0.05

that the U value is significantly smaller in magnitude with the inclusion of spin-orbit coupling. A possible justification for this behavior is the introduction of orbital contributions to the total localized magnetic moments with the inclusion of spin-orbit coupling [22, 81].

1. *Canting angle exploration*

In order to explore the effects of Hubbard and Hund parameters on the energetics of non-collinear magnetic structure, we calculated the energy as a function of constrained canting angle, which has been experimentally measured for $LiNiPO_4$ [79]. The non-collinear magnetic constraints were performed in VASP in accordance with the method developed by Ma and Dudarev [82]. We used the experimentally derived spin canted structure as a reference provided by the Bilbao Crystallographic Server, as shown in Figure 4 [79, 80]. The energy versus canting angle curve is shown in Figure 5a. We found that the stable canting direction is in the opposite direction to the experimentally measured canting angle. However, this discrepancy with experiment was limited to the canting direction; the computed stable magnetic structure still obeyed the symmetry of the *Pnm'a* magnetic space group.

Similarly to the work by Bousquet and Spaldin [19], we observe an increasing canting angle with Hund J value. Interestingly, adding a U and J correction to O-p results in a slightly decreased stable canting angle. However, we find that in all cases, the computed stable canting angle is significantly less than the experimentally measured canting angle of 7.8 degrees [79].

The constraining effective site magnetic field, $\vec{H}_i^{\text{eff}}$, can be described as the following

$$\vec{H}_i^{\text{eff}} = 2\lambda \left[\vec{M}_i - \hat{M}_i^0 \left(\hat{M}_i^0 \cdot \vec{M}_i \right) \right], \tag{13}$$

where $\vec{M}_i$ are the integrated magnetic moments at site i, and $\hat{M}_i^0$ are the unit vectors pointing in the individual site constraining directions [82]. The x component of the constraining field (in the direction of canting), $H_{i,x}^{\text{eff}}$, is plotted versus the constraining angle in Figure 5b. We see that where $H_{i,x}^{\text{eff}}$ changes sign corresponds to the minimum of Figure 5a.

2. *Effect of U and J values on geometry optimization*

While the addition of Hubbard and Hund parameters go some way to addressing the canting angle of $LiNiPO_4$, introducing these terms can also alter the geometry of the system. To explore this effect, we performed structural relaxations of the system with various combinations of Hubbard and Hund corrections. In each of the structural relaxation calculations, a maximum force tolerance of 10 meV/Å was used. The Hubbard U and Hund J values used include those calculated using linear response, which are approximations of the values that are reported in Table III. Additionally, we tested the Ni-d U and J values used in Ref. 19. All calculations included spin-orbit coupling, and were constrained to the experimentally observed canting angle (7.8 degrees).

Table IV lists the optimized unit cell parameters and volume, compared with the experimentally measured geometry [79]. For both the PBE+U_{eff} and PBE+U+J schemes, adding corrections to the Ni-d space worsens the geometry relative to the uncorrected PBE geometry (as earlier observed by Zhou and co-workers [29]). However, the further addition of corrections to the O-p subspace reduces the errors by three-fold, resulting in geometries that are closest to experiment. This is similar to observations in other studies when applying corrections to O-p subspaces [5, 45]. We note that applying a $+J$ correction to non-magnetic O-p states may seem unconventional. However, it should be stressed that this correction is for localized static correlation error effects that do not vanish at zero magnetization. Nor, indeed, does the introduction of $+J$ necessarily induce magnetization, and the projected magnetic moments on $LiNiPO_4$ remain just below 0.01 μ_B, with and without on-site corrections to O-2p states. Meanwhile, we can see that adding a $+J$ parameter does not significantly alter the cell parameters.

3. *Discussion on TM-O bond length versus* U, J, *and* V *corrections*

Table IV also presents the change in mean Ni-O bond length between nearest-neighbor pairs for various on-site corrections. For the Ni-O bond length it is the same story as for the cell parameters: applying U and J to the Ni-d sites worsens the results relative to the PBE result, but by applying corrections to the O-p channels we obtain bond lengths that are in closer agreement with experiment. In Ref. 5, some of us attempted to rationalize this trend in the computed bond length between transition metal species and oxygen anions and how it improves with the introduction of corrections to the O-p subspace. We suggested that when $+U$ is added to the Ni-d subspace the resulting shift in the potential disrupts hybridization between the Ni-d and O-p orbitals, weakening the bonding between these two elements (and thus leading to bond lengthening). Applying corrections to the O-p re-aligns these two subspaces and allows them

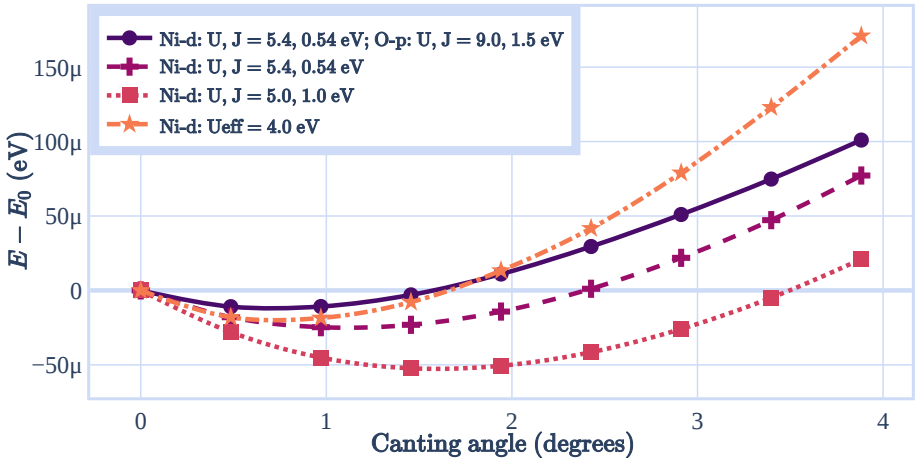

(a) Computed energy versus constraining canting angle

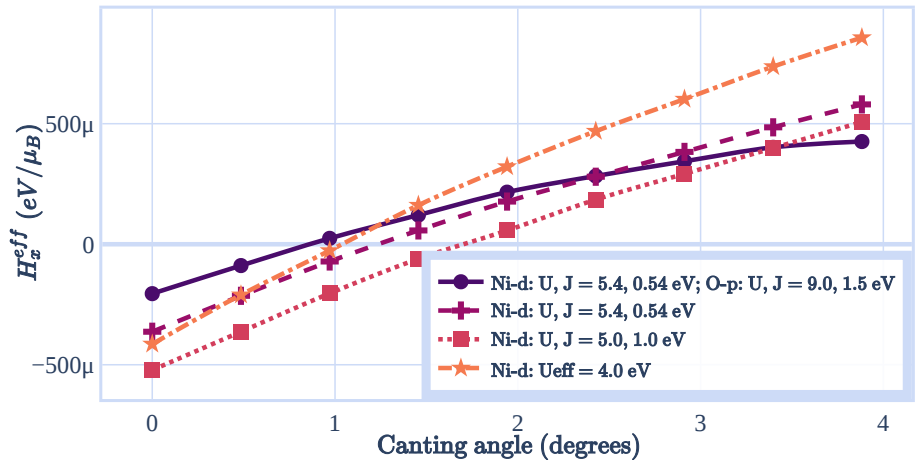

(b) Effective constraining field versus constraining canting angle

FIG. 5: (a) Computed relative energy and (b) x-component of effective constraining local magnetic field for various Hubbard and Hund on-site corrections applied to the Ni-d and O-p manifolds.

TABLE IV: Lattice parameters, cell volume, and mean Ni-O bond length (d) of $LiNiPO_4$ canted structure for different Hubbard U and Hund J corrections

method	Ni-d (eV)	O-p (eV)	a (Å)	b (Å)	c (Å)	volume (Å^3)	d (Å)
experiment			10.03	5.85	4.68	274.93	2.086 ± 0.044
PBE			10.09 (+0.6%)	5.92 (+1.1%)	4.72 (+0.9%)	282.09 (+2.6%)	2.099 ± 0.037
PBE+U_{eff}	$U_{\text{eff}} = 4$	$U_{\text{eff}} = 0$	10.14 (+1.1%)	5.92 (+1.1%)	4.73 (+1.0%)	283.71 (+3.2%)	
		$U_{\text{eff}} = 7.5$	10.07 (+0.4%)	5.87 (+0.3%)	4.69 (+0.3%)	277.56 (+1.0%)	
PBE+U+J	$U = 5$	U, $J = 0$	10.15 (+1.2%)	5.92 (+1.1%)	4.73 (+1.0%)	284.19 (+3.4%)	2.108 ± 0.039
	$J = 1$	U, $J = 9$, 1.5	10.07 (+0.4%)	5.88 (+0.4%)	4.69 (+0.3%)	277.86 (+1.1%)	2.095 ± 0.043

to "re-hybridize." The DMFT community has sought to address these issues with other approaches, including by tweaking the double-counting term or by using results from GW [83, 84].

In an attempt to more thoroughly explore this reasoning, Figure 6 provides a comparison for the projected density of states (DOS) of $LiNiPO_4$ for PBE and PBE+U+J (with and without corrections to O-p). It is difficult to discern re-hybridization from these DOS plots alone.

Without an explicit quantification of hybridization effects, we have added a derivation in the Supplementary Information [77] that presents a mathematical expression of the forces acting on ions due to +U+V corrections. This result is an extension of the theory put forth

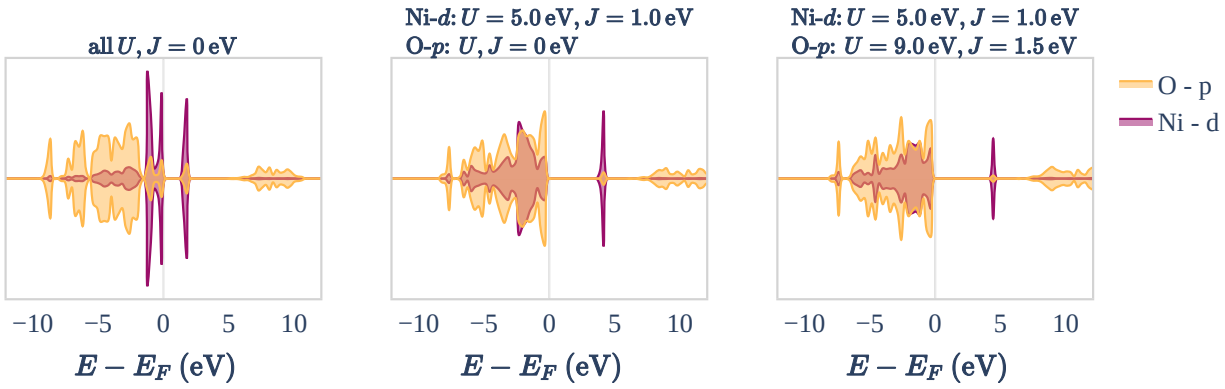

FIG. 6: Projected electronic density of states for $LiNiPO_4$ (calculated using experimental unit cell [79]) without Hubbard or Hund corrections applied, as well as $+U$ and $+J$ applied to Ni-d channels, and both Ni-d and O-p states, respectively.

by Matteo Cococcioni in Section 4.1 of Ref. 10. We argue that in quantifying the forces on TM-O bond lengths due to on-site corrections, it is possible to show that the force contributions due to both $+U^{\gamma}$ and $+V^{\gamma\gamma'}$ can, and should, be treated on the same footing, where γ and γ' correspond to atomic sites. It isn't possible to definitively state the comparative magnitude, or sign, of these force contributions without additional calculations or simplifications based on physical intuition. However, the result suggests that the forces on TM-O bond-length due to O-p U values will have a comparative magnitude to the forces due to inter-site Coulomb corrections from $+V$.

In the Supplementary Information [77], we further hypothesize the sign of these force contributions, starting from a DFT geometry-optimized structure without on-site corrections. Using these assumptions, which are based on computational trends in bulk TMOs, we conclude that either applying a $+U$ correction to the O-p manifold or a $+V$ between TM and O states mitigates the overestimation of TM-O bond lengths that arise when applying $+U$ to localized states around the TM species.

IV. CONCLUSIONS

This study provides a high-throughput `atomate` framework for calculating Hubbard U and Hund J values. Using the spin-polarized linear-response methodology [5], we generated a database of U and J values for over one thousand transition-metal-containing materials. This enabled the creation of a "periodic table" of U and J distributions, where for each element we observe a range of Hubbard U and Hund J values. These distributions exhibited clustering depending on the corresponding m_l and n_l values, but these quantities alone do not prove sufficient to predict the Hubbard and Hund parameters.

In order to investigate inter-site screening effects on the resulting U/J values, we performed a small supercell scaling study for the full screening linear response analysis for NiO, in addition to the conventional, atom-wise, screening. This exploration can be found in the Supplementary Information [77], and the details of the full screening matrix inversion can be found in Appendix A. We found that the full matrix inversion is much more sensitive to the size of the unit cell compared to the conventional, atom-wise screening. The theoretical reasons for this phenomenon will be an interesting pursuit for future studies.

In order to test the validity of the linear response implementation, we explored the spin-canting non-collinear magnetic structure and unit cell shape of $LiNiPO_4$, and compare the results with previous experimental [79] and computational [19, 29] studies. Similarly to Bousquet and Spaldin [19], we observed that the computed stable canting angle was less than 50% of the experimentally measured canting angle of nickel magnetic moments in olivine $LiNiPO_4$ for all Ni-d Hund J values tested. We also observed that the canting angle was very sensitive to the Hund's J values. This confirms that Hund J values are crucial for exploring the properties of transition metal oxides which exhibit a non-collinear magnetic structure. In addition to the canting structure of $LiNiPO_4$, we examined the optimal unit cell geometry for various Hubbard U and Hund J corrections. While applying a $+U+J$ correction to Ni-d resulted in increased disagreement with experimentally measured unit cell parameters [29], applying an on-site Hubbard/Hund correction to O-p occupancies greatly improved the agreement of unit cell shape with experiment [79]. This finding reinforces the importance of including a $+U+J$ correction to oxygen sites in order to resolve the accurate bonding behavior between transition metal species and neighboring oxygen atoms.

ACKNOWLEDGEMENTS

The authors would like to thank Matteo Cococcioni for helpful correspondence, and for addressing questions on the original linear response methodology. G.M. acknowledges support from the Department of Energy Computational Science Graduate Fellowship (DOE CSGF) under grant DE-SC0020347. E.L. acknowledges support from the Swiss National Science Foundation (SNSF) under grant 200021-179138. D.O'R. acknowledges the support of Science Foundation Ireland (SFI) [19/EPSRC/3605 & 12/RC/2278_2], the Engineering and Physical Sciences Research Council [EP/S030263/1], and the European Regional Development Fund under the SFI AMBER award. Computations in this paper were performed using resources of the National Energy Research Scientific Computing Center (NERSC), a U.S. Department of Energy Office of Science User Facility operated under contract no. DE-AC02-05CH11231. Expertise in high-throughput calculations, data and software infrastructure was supported by the U.S. Department of Energy, Office of Science, Office of Basic Energy Sciences, Materials Sciences and Engineering Division under Contract DE-AC02-05CH11231: Materials Project program KC23MP.

CREDIT TAXONOMY

We highlight the author contributions to this study using the CRediT taxonomy. **Guy C. Moore**: Conceptualization, Methodology, Software, Validation, Formal analysis, Investigation, Data Curation, Writing - Original Draft, Writing - Review & Editing, Visualization **Matthew K. Horton**: Conceptualization, Software, Validation, Investigation, Writing - Review & Editing, Visualization, Project administration **Edward Linscott**: Methodology, Validation, Formal analysis, Investigation, Writing - Review & Editing **Alexander M. Ganose**: Software, Writing - Review & Editing **Martin Siron**: Software, Writing - Review & Editing **David D. O'Regan**: Methodology, Validation, Formal analysis, Investigation, Writing - Review & Editing **Kristin A. Persson**: Writing - Review & Editing, Supervision, Project administration.

Appendix A: Screening matrix inversions

Below are the matrix representations of the response matrices at each level of response matrix inversiooutlined by Linscott and others for a system with two Hubbard sites [5].

Point-wise 1×1 inversion:

$$\chi^{-1} = \begin{pmatrix} 1/\chi_{11} & 0 \\ 0 & 1/\chi_{22} \end{pmatrix} \tag{A1}$$

Atom-wise (conventional) 2×2 inversion:

$$\chi^{-1} = \begin{pmatrix} \chi_{11} & \chi_{12} \\ \chi_{21} & \chi_{22} \end{pmatrix}^{-1} \tag{A2}$$

We can extend this formalism to the multiple site (multi-site) responses by considering the response matrix for two sites, χ_{ij}, where i and j are the site indices.
Point-wise inversion:

$$\chi^{-1} = \begin{pmatrix} \begin{pmatrix} 1/\chi_{11}^{\uparrow\uparrow} & 0 \\ 0 & 1/\chi_{11}^{\downarrow\downarrow} \end{pmatrix} & 0 \\ 0 & \begin{pmatrix} 1/\chi_{22}^{\uparrow\uparrow} & 0 \\ 0 & 1/\chi_{22}^{\downarrow\downarrow} \end{pmatrix} \end{pmatrix} \tag{A3}$$

Atom-wise (conventional) inversion:

$$\chi^{-1} = \begin{pmatrix} \begin{pmatrix} \chi_{11}^{\uparrow\uparrow} & \chi_{11}^{\uparrow\downarrow} \\ \chi_{11}^{\downarrow\uparrow} & \chi_{11}^{\downarrow\downarrow} \end{pmatrix}^{-1} & 0 \\ 0 & \begin{pmatrix} \chi_{22}^{\uparrow\uparrow} & \chi_{22}^{\uparrow\downarrow} \\ \chi_{22}^{\downarrow\uparrow} & \chi_{22}^{\downarrow\downarrow} \end{pmatrix}^{-1} \end{pmatrix} \tag{A4}$$

Full inversion:

$$\chi^{-1} = \begin{pmatrix} \chi_{11}^{\uparrow\uparrow} & \chi_{11}^{\uparrow\downarrow} & \chi_{12}^{\uparrow\uparrow} & \chi_{12}^{\uparrow\downarrow} \\ \chi_{11}^{\downarrow\uparrow} & \chi_{11}^{\downarrow\downarrow} & \chi_{12}^{\downarrow\uparrow} & \chi_{12}^{\downarrow\downarrow} \\ \chi_{21}^{\uparrow\uparrow} & \chi_{21}^{\uparrow\downarrow} & \chi_{22}^{\uparrow\uparrow} & \chi_{22}^{\uparrow\downarrow} \\ \chi_{21}^{\downarrow\uparrow} & \chi_{21}^{\downarrow\downarrow} & \chi_{22}^{\downarrow\uparrow} & \chi_{22}^{\downarrow\downarrow} \end{pmatrix}^{-1} \tag{A5}$$

We note that in the latter case, when performing a spin-polarize linear response calculation, one constructs a $2N \times 2N$ response matrix where N is the number of Hubbard sites (or $N \times N$ in the case of non-spin-polarized linear response). For bulk systems often several Hubbard sites will be equivalent, and one can save computational time by performing linear response calculations for the set of inequivalent sites, and then populating the response matrix for all equivalent Hubbard-site pairs.

Appendix B: Post-processing & uncertainty quantification

In order to extract the response matrices from the raw DFT data, curve fitting was performed using a least-squares polynomial fit implemented in `numpy` [85]. The uncertainty associated with each computed slope was obtained from the covariance matrix produced as a result of the least-squares fit. These uncertainty values were then utilized to determine the errors associated with the Hubbard U and Hund J values. The error quantification was performed by computing the propagation of uncertainty based on the Jacobian of each scaling formula for Hubbard U and Hund J. This method for error propagation is general to multiple levels of screening between

element	U			J		
	mean	σ	N	mean	σ	N
V	4.123	0.471	84	0.599	0.162	84
Mn	4.792	0.830	63	0.740	0.246	63
Cu	7.773	1.251	61	1.366	0.932	61
Fe	4.659	0.826	55	0.279	0.378	55
Ti	4.907	0.481	53	0.635	0.185	53
Cr	2.906	0.471	46	0.611	0.135	46
Nb	0.536	0.157	43	0.241	0.082	43
W	1.844	0.252	42	0.423	0.043	42
Zn	1.917	0.564	40	1.790	0.456	40
Co	5.159	0.608	31	0.560	0.292	31
Ni	5.849	0.797	31	0.682	0.186	31
Ta	3.733	0.164	30	0.668	0.041	30
Zr	4.199	0.244	28	0.907	0.091	28
Ag	2.254	0.852	25	1.236	0.256	25
Mo	2.561	0.321	23	0.483	0.062	23
Hg	0.521	0.142	20	0.429	0.032	20
Re	0.620	0.233	19	0.269	0.103	19
Cd	0.238	0.469	19	0.632	0.097	19
Sc	1.921	0.352	17	1.169	0.396	17
Y	4.302	0.343	17	1.694	0.361	17
Hf	3.515	0.229	13	1.085	0.167	13
Ru	3.000	0.371	11	0.506	0.146	11
Pt	1.554	0.315	10	0.447	0.041	10
Os	1.911	0.440	8	0.392	0.078	8
Pd	3.757	0.899	7	0.691	0.063	7
Au	1.120	0.248	6	0.495	0.034	6
Rh	1.528	0.196	5	0.457	0.056	5
Ir	1.902	0.095	4	0.315	0.324	4
Tc	2.946	0.012	3	0.580	0.004	3
Total			814			814

TABLE V: The mean and standard deviation (σ) in the U and J parameters used in the periodic tables of Figure 1, alongside the number of samples N.

spin, site, and orbital responses.

We begin by considering the following screening matrix introduced in Equation 11, from which Hubbard U and Hund J values are derived [5]

$$f_{ij} = \left(\chi_0^{-1} - \chi^{-1}\right)_{ij}$$

Derivatives of the χ^{-1} matrix with respect to individual χ_{kl} can be obtained by the following relation:

$$\frac{\partial}{\partial \chi_{kl}}\left(\chi^{-1}\right) = -\chi^{-1}\left(\frac{\partial}{\partial \chi_{kl}}\chi\right)\chi^{-1}$$

$$\text{where } \frac{\partial}{\partial \chi_{kl}}\{\chi\}_{ij} = \begin{cases} 1 & \text{if } kl = ij \\ 0 & \text{otherwise} \end{cases}$$

$$\frac{\partial}{\partial \chi_{kl}}\left\{\chi^{-1}\right\}_{ij} = -\left\{\chi^{-1}\right\}_{ik}\left\{\chi^{-1}\right\}_{lj} \tag{B1}$$

Using this fact, it is possible to obtain the full Jacobian of f with respect to response χ matrices which can be used to obtain the covariance uncertainty matrix associated with the elements of f_{ij}, to a first-order expansion of f_{ij} [86]

$$\boldsymbol{\Sigma}_f = \boldsymbol{J}_{\chi_0}\boldsymbol{\Sigma}_{\chi_0}\boldsymbol{J}_{\chi_0}^T + \boldsymbol{J}_{\chi}\boldsymbol{\Sigma}_{\chi}\boldsymbol{J}_{\chi}^T \tag{B2}$$

where $\boldsymbol{\Sigma}_f$ is a $N^2 \times N^2$ matrix (f is $N \times N$). Each element of $\boldsymbol{\Sigma}_f$, $\left\{\Sigma_f\right\}_{ij,kl}$, corresponds to the covariance between f_{ij} and f_{kl} matrix elements. $\boldsymbol{\Sigma}_{\chi}$ and $\boldsymbol{\Sigma}_{\chi_0}$ are the covariance matrices for each $\{\chi\}_{kl}$ and $\{\chi_0\}_{kl}$, and the diagonal elements are populated using the squared uncertainty values associated with the slopes fit to the response data. In addition, $\boldsymbol{J}_{\chi}$ and $\boldsymbol{J}_{\chi_0}$ are the symbolically derived Jacobians corresponding to each response value, as proposed in Equation B1. Assuming that the individual elements of χ and χ_0 are independent, we can assume that $\boldsymbol{\Sigma}$ covariance matrices are diagonal in order to make the following simplification:

$$\sigma^2(f_{ij}) = \sum_{kl}\left(\frac{\partial}{\partial\{\chi_0\}_{kl}}f_{ij}\right)^2\sigma^2(\{\chi_0\}_{kl}) + \sum_{kl}\left(\frac{\partial}{\partial\{\chi\}_{kl}}f_{ij}\right)^2\sigma^2(\{\chi\}_{kl}), \tag{B3}$$

where $\sigma^2(f_{ij})$, $\sigma^2(\{\chi_0\}_{ij})$, and $\sigma^2(\{\chi\}_{ij})$ correspond to the diagonal elements of $\boldsymbol{\Sigma}_f$, $\boldsymbol{\Sigma}_{\chi_0}$, and $\boldsymbol{\Sigma}_{\chi}$, respectively.

With the established expression for the uncertainty values of f in Equation B3, we can express the squared uncertainty of U, for an atomic site γ, in the next level of uncertainty propagation,

$$\sigma^2(U^{\gamma}) = \sum_{\sigma,\sigma'}\left(\frac{\partial}{\partial f_{\gamma\gamma}^{\sigma\sigma'}}G_U(f_{\gamma\gamma})\right)^2\sigma^2(f_{\gamma\gamma}^{\sigma\sigma'}). \tag{B4}$$

Equation B4 can be extended to an expression of the squared uncertainty of Hund J, where G_U and G_J are functions of 2×2 sub-matrices along the diagonal of f, as introduced in Equation 11, and depend on the different scaling schemes introduced in Ref. 5. The results of this error analysis are shown in Table V.

Appendix C: VASP precision issue

We found that for some closed-shell systems, such as those containing Zn, the I/O precision of the occupation numbers in VASP had a significant effect on the resulting linear response analysis. This is because the change in occupation number on Zn-d states induced by the on-site potential was on the same order of magnitude as the precision cutoff itself. For this reason, we created a very basic patch to the VASP version 6.2.1 source code to increase the precision of occupation numbers and site magnetization written in the VASP `OUTCAR` file.

Using this higher precision, we found that the U and

J calculated using linear response for Zn-d were 2.3±0.1 eV and 1.7±0.0 eV, respectively. This is in stark contrast to the original VASP code I/O precision, which wrongly produced U, $J = 0.0$ eV.

[1] E. Koch, F. Anders, and M. Jarrell, *Correlated electrons: from models to materials*, edited by E. Pavarini, Schriften des Forschungszentrums Jülich. Reihe modeling and simulation, Vol. 2 (Forschungszentrum Jülich GmbH Zentralbibliothek, Verlag, Jülich, 2012) p. getr. Paginierung, record converted from JUWEL: 18.07.2013.

[2] D. C. Langreth and M. J. Mehl, Beyond the local-density approximation in calculations of ground-state electronic properties, Phys. Rev. B **28**, 1809 (1983).

[3] W. Kohn and L. J. Sham, Self-consistent equations including exchange and correlation effects, Phys. Rev. **140**, A1133 (1965).

[4] M. Cococcioni and S. de Gironcoli, Linear response approach to the calculation of the effective interaction parameters in the LDA+U method, Phys. Rev. B **71**, 035105 (2005).

[5] E. B. Linscott, D. J. Cole, M. C. Payne, and D. D. O'Regan, Role of spin in the calculation of Hubbard U and Hund's J parameters from first principles, Phys. Rev. B **98**, 235157 (2018).

[6] V. I. Anisimov, J. Zaanen, and O. K. Andersen, Band theory and Mott insulators: Hubbard U instead of Stoner I, Phys. Rev. B **44**, 943 (1991).

[7] V. I. Anisimov, I. V. Solovyev, M. A. Korotin, M. T. Czyżyk, and G. A. Sawatzky, Density-functional theory and NiO photoemission spectra, Phys. Rev. B **48**, 16929 (1993).

[8] V. I. Anisimov, F. Aryasetiawan, and A. I. Lichtenstein, First-principles calculations of the electronic structure and spectra of strongly correlated systems: The LDA+U method, J. Phys. Condens. Matter **9**, 767 (1997).

[9] W. E. Pickett, S. C. Erwin, and E. C. Ethridge, Reformulation of the LDA+U method for a local-orbital basis, Phys. Rev. B **58**, 1201 (1998).

[10] M. Cococcioni, Chapter 4 - The LDA+U approach: A simple hubbard correction for correlated ground states, in [1], pp. 4.1–4.40, record converted from JUWEL: 18.07.2013.

[11] H. J. Kulik, M. Cococcioni, D. A. Scherlis, and N. Marzari, Density Functional Theory in Transition-Metal Chemistry: A Self-Consistent Hubbard U Approach, Physical Review Letters **97**, 103001 (2006).

[12] B. Himmetoglu, A. Floris, S. d. Gironcoli, and M. Cococcioni, Hubbard-corrected DFT energy functionals: The LDA+U description of correlated systems, International Journal of Quantum Chemistry **114**, 14 (2014).

[13] A. Bajaj, J. P. Janet, and H. J. Kulik, Communication: Recovering the flat-plane condition in electronic structure theory at semi-local DFT cost, The Journal of Chemical Physics **147**, 191101 (2017), publisher: American Institute of Physics.

[14] A. Bajaj and H. J. Kulik, Molecular DFT+U: A Transferable, Low-Cost Approach to Eliminate Delocalization Error, The Journal of Physical Chemistry Letters 10.1021/acs.jpclett.1c00796 (2021), publisher: American Chemical Society.

[15] V. L. Campo and M. Cococcioni, Extended DFT+U+V method with on-site and inter-site electronic interactions, Journal of Physics: Condensed Matter **22**, 055602 (2010).

[16] N. Tancogne-Dejean and A. Rubio, Parameter-free hybridlike functional based on an extended Hubbard model: DFT+U+V, Physical Review B **102**, 155117 (2020).

[17] S.-H. Lee and Y.-W. Son, First-principles approach with a pseudohybrid density functional for extended Hubbard interactions, Physical Review Research **2**, 043410 (2020).

[18] S. L. Dudarev, G. A. Botton, S. Y. Savrasov, C. J. Humphreys, and A. P. Sutton, Electron-energy-loss spectra and the structural stability of nickel oxide: An LSDA+U study, Phys. Rev. B **57**, 1505 (1998).

[19] E. Bousquet and N. Spaldin, J dependence in the LSDA+U treatment of noncollinear magnets, Phys. Rev. B **82**, 220402 (2010).

[20] F. Bultmark, F. Cricchio, O. Grånäs, and L. Nordström, Multipole decomposition of LDA+U energy and its application to actinide compounds, Phys. Rev. B **80**, 035121 (2009).

[21] S. L. Dudarev, P. Liu, D. A. Andersson, C. R. Stanek, T. Ozaki, and C. Franchini, Parametrization of LSDA+U for noncollinear magnetic configurations: Multipolar magnetism in UO_2, Phys. Rev. Mater. **3**, 083802 (2019).

[22] S. V. Streltsov and D. I. Khomskii, Orbital physics in transition metal compounds: new trends, Physics-Uspekhi **60**, 1121 (2017), publisher: IOP Publishing.

[23] T. A. Mellan, F. Corà, R. Grau-Crespo, and S. Ismail-Beigi, Importance of anisotropic coulomb interaction in $LaMnO_3$, Phys. Rev. B **92**, 085151 (2015).

[24] A. Georges, L. d. Medici, and J. Mravlje, Strong correlations from Hund's coupling, Annual Review of Condensed Matter Physics **4**, 137 (2013), https://doi.org/10.1146/annurev-conmatphys-020911-125045.

[25] H. C. Herper, T. Ahmed, J. M. Wills, I. Di Marco, T. Björkman, D. Iuşan, A. V. Balatsky, and O. Eriksson, Combining electronic structure and many-body theory with large databases: A method for predicting the nature of $4f$ states in Ce compounds, Physical Review Materials **1**, 033802 (2017).

[26] A. Jain, G. Hautier, S. P. Ong, C. J. Moore, C. C. Fischer, K. A. Persson, and G. Ceder, Formation enthalpies by mixing GGA and GGA+U calculations, Physical Review B **84**, 045115 (2011), publisher: American Physical Society.

[27] M. Yu, M. Yang, C. Wu, and N. Marom, Machine learning the Hubbard U parameter in DFT+U using Bayesian optimization, npj Computational Materials **6**, 1 (2020), number: 1 Publisher: Nature Publishing Group.

[28] R. C. Albers, N. E. Christensen, and A. Svane, Hubbard-U band-structure methods, Journal of Physics: Condensed Matter **21**, 343201 (2009).

[29] F. Zhou, M. Cococcioni, C. A. Marianetti, D. Morgan, and G. Ceder, First-principles prediction of redox potentials in transition-metal compounds with LDA+U, Phys. Rev. B **70**, 235121 (2004).

[30] Y.-C. Wang, Z.-H. Chen, and H. Jiang, The local projec-

tion in the density functional theory plus U approach: A critical assessment, The Journal of Chemical Physics **144**, 144106 (2016).
[31] X. Ren, Chapter 2 - The random phase approximation and its applications to real materials (Forschungszentrum Jülich GmbH Zentralbibliothek, Verlag, Jülich, 2019) pp. 2.1–2.27.
[32] L. Vaugier, H. Jiang, and S. Biermann, Hubbard U and hund exchange J in transition metal oxides: Screening versus localization trends from constrained random phase approximation, Phys. Rev. B **86**, 165105 (2012).
[33] A. J. Cohen, P. Mori-Sánchez, and W. Yang, Insights into current limitations of density functional theory, Science **321**, 792 (2008).
[34] A. C. Burgess, E. Linscott, and D. D. O'Regan, DFT+U-type functional derived to explicitly address the flat plane condition, Phys. Rev. B **107**, L121115 (2023).
[35] Q. Zhao, E. I. Ioannidis, and H. J. Kulik, Global and local curvature in density functional theory, J. Chem. Phys. **145**, 054109 (2016).
[36] A. Jain, S. P. Ong, G. Hautier, W. Chen, W. D. Richards, S. Dacek, S. Cholia, D. Gunter, D. Skinner, G. Ceder, and K. Persson, The Materials Project: A materials genome approach to accelerating materials innovation, APL Mater. **1**, 011002 (2013).
[37] S. P. Ong, GGA+U calculations, `https://docs.materialsproject.org/methodology/gga-plus-u/`.
[38] `MPContribs` Hubbard on-site corrections, `https://contribs.materialsproject.org/projects/hubbard` (2023).
[39] A. I. Liechtenstein, V. I. Anisimov, and J. Zaanen, Density functional theory and strong interactions: Orbital ordering in Mott-Hubbard insulators, Phys. Rev. B **52**, R5467 (1995).
[40] L. Binci and N. Marzari, Noncollinear DFT+U and Hubbard parameters with fully-relativistic ultrasoft pseudopotentials (2023), arXiv:2304.10178 [cond-mat].
[41] J. E. Peralta, G. E. Scuseria, and M. J. Frisch, Noncollinear magnetism in density functional calculations, Phys. Rev. B **75**, 125119 (2007).
[42] B. Himmetoglu, R. M. Wentzcovitch, and M. Cococcioni, First-principles study of electronic and structural properties of CuO, Phys. Rev. B **84**, 115108 (2011).
[43] I. V. Solovyev, P. H. Dederichs, and V. I. Anisimov, Corrected atomic limit in the local-density approximation and the electronic structure of d impurities in Rb, Phys. Rev. B **50**, 16861 (1994).
[44] J. Hafner and G. Kresse, The Vienna Ab-Initio Simulation Program VASP: An Efficient and Versatile Tool for Studying the Structural, Dynamic, and Electronic Properties of Materials, in *Properties of Complex Inorganic Solids*, edited by A. Gonis, A. Meike, and P. E. A. Turchi (Springer US, Boston, MA, 1997) pp. 69–82.
[45] D. S. Lambert and D. D. O'Regan, Use of DFT+U+J with linear response parameters to predict non-magnetic oxide band gaps with hybrid-functional accuracy, Phys. Rev. Res. **5**, 013160 (2023).
[46] K. Mathew, J. H. Montoya, A. Faghaninia, S. Dwarakanath, M. Aykol, H. Tang, I. Chu, T. Smidt, B. Bocklund, M. K. Horton, J. Dagdelen, B. Wood, Z. Liu, J. Neaton, S. P. Ong, K. A. Persson, and A. Jain, Atomate: A high-level interface to generate, execute, and analyze computational materials science workflows, Computational Materials Science **139**, 140 (2017).
[47] J. P. Perdew, K. Burke, and M. Ernzerhof, Generalized gradient approximation made simple, Phys. Rev. Lett. **77**, 3865 (1996).
[48] `pymatgen` code repository, `https://github.com/materialsproject/pymatgen.git` (2023).
[49] J. W. Bennett, B. G. Hudson, I. K. Metz, D. Liang, S. Spurgeon, Q. Cui, and S. E. Mason, A systematic determination of Hubbard U using the GBRV ultrasoft pseudopotential set, Computational Materials Science **170**, 109137 (2019).
[50] `atomate` code repository, `https://github.com/hackingmaterials/atomate.git` (2023).
[51] M. K. Horton, J. H. Montoya, M. Liu, and K. A. Persson, High-throughput prediction of the ground-state collinear magnetic order of inorganic materials using Density Functional Theory, NPG Computational Materials **5**, 1 (2019), number: 1 Publisher: Nature Publishing Group.
[52] E. Goh, J. Mah, and T. Yoon, Effects of Hubbard term correction on the structural parameters and electronic properties of wurtzite ZnO, Computational Materials Science **138**, 111 (2017).
[53] N. Bondarenko, O. Eriksson, and N. V. Skorodumova, Polaron mobility in oxygen-deficient and lithium-doped tungsten trioxide, Phys. Rev. B **92**, 165119 (2015).
[54] J. J. Plata, A. M. Márquez, and J. F. Sanz, Communication: Improving the density functional theory $+u$ description of CeO_2 by including the contribution of the O $2p$ electrons, The Journal of Chemical Physics **136**, 041101 (2012).
[55] F. Kuang, S. Kang, X. Kuang, and Q. Chen, An ab initio study on the electronic and magnetic properties of MgO with intrinsic defects, RSC Adv. **4**, 51366 (2014).
[56] H. A. Kramers, L'interaction Entre les Atomes Magnétogènes dans un Cristal Paramagnétique, Physica **1**, 182 (1934).
[57] P. W. Anderson, Antiferromagnetism. Theory of Superexchange Interaction, Physical Review **79**, 350 (1950).
[58] P. Virtanen, R. Gommers, T. E. Oliphant, M. Haberland, T. Reddy, D. Cournapeau, E. Burovski, P. Peterson, W. Weckesser, J. Bright, S. J. van der Walt, M. Brett, J. Wilson, K. J. Millman, N. Mayorov, A. R. J. Nelson, E. Jones, R. Kern, E. Larson, C. J. Carey, İ. Polat, Y. Feng, E. W. Moore, J. VanderPlas, D. Laxalde, J. Perktold, R. Cimrman, I. Henriksen, E. A. Quintero, C. R. Harris, A. M. Archibald, A. H. Ribeiro, F. Pedregosa, P. van Mulbregt, and SciPy 1.0 Contributors, SciPy 1.0: Fundamental Algorithms for Scientific Computing in Python, Nature Methods **17**, 261 (2020).
[59] L. Wang, T. Maxisch, and G. Ceder, Oxidation energies of transition metal oxides within the GGA+U framework, Phys. Rev. B **73**, 195107 (2006).
[60] A. Wang, R. Kingsbury, M. McDermott, M. Horton, A. Jain, S. P. Ong, S. Dwaraknath, and K. A. Persson, A framework for quantifying uncertainty in dft energy corrections, Scientific Reports **11**, 15496 (2021).
[61] D. van der Marel and G. A. Sawatzky, Electron-electron interaction and localization in d and f transition metals, Physical Review B **37**, 10674 (1988), publisher: American Physical Society.
[62] I. S. Elfimov, A. Rusydi, S. I. Csiszar, Z. Hu, H. H. Hsieh, H.-J. Lin, C. T. Chen, R. Liang, and G. A. Sawatzky, Magnetizing Oxides by Substituting Nitrogen for Oxygen, Physical Review Letters **98**, 137202 (2007).

[63] R. G. Parr and R. G. Pearson, Absolute hardness: companion parameter to absolute electronegativity, Journal of the American Chemical Society **105**, 7512 (1983).

[64] X. Dong, A. R. Oganov, H. Cui, X.-F. Zhou, and H.-T. Wang, Electronegativity and chemical hardness of elements under pressure, Proceedings of the National Academy of Sciences **119**, e2117416119 (2022).

[65] D. Guerra, R. Contreras, P. Pérez, and P. Fuentealba, Hardness and softness kernels, and related indices in the spin polarized version of density functional theory, Chemical Physics Letters **419**, 37 (2006).

[66] C. Ricca, I. Timrov, M. Cococcioni, N. Marzari, and U. Aschauer, Self-consistent site-dependent DFT+U study of stoichiometric and defective $SrMnO_3$, Phys. Rev. B **99**, 094102 (2019).

[67] D. Lu and P. Liu, Rationalization of the Hubbard U parameter in CeO_x from first principles: Unveiling the role of local structure in screening, The Journal of Chemical Physics **140**, 084101 (2014), https://doi.org/10.1063/1.4865831.

[68] I. D. Brown, Recent developments in the methods and applications of the bond valence model, Chemical Reviews **109**, 6858 (2009), pMID: 19728716, https://doi.org/10.1021/cr900053k.

[69] L. Ward, A. Dunn, A. Faghaninia, N. E. Zimmermann, S. Bajaj, Q. Wang, J. Montoya, J. Chen, K. Bystrom, M. Dylla, K. Chard, M. Asta, K. A. Persson, G. J. Snyder, I. Foster, and A. Jain, Matminer: An open source toolkit for materials data mining, Computational Materials Science **152**, 60 (2018).

[70] T. Lam Pham, H. Kino, K. Terakura, T. Miyake, K. Tsuda, I. Takigawa, and H. Chi Dam, Machine learning reveals orbital interaction in materials, Science and Technology of Advanced Materials **18**, 756 (2017).

[71] M. Karamad, R. Magar, Y. Shi, S. Siahrostami, I. D. Gates, and A. Barati Farimani, Orbital graph convolutional neural network for material property prediction, Physical Review Materials **4**, 093801 (2020).

[72] J. C. Slater, *Quantum theory of atomic structure*, International series in pure and applied physics (McGraw-Hill, New York, 1960).

[73] N. W. Ashcroft and D. N. Mermin, *Solid state physics* (Brooks/Cole, Australia, 1976 - 1976).

[74] J. H. Yang, T. Chen, L. Barroso-Luque, Z. Jadidi, and G. Ceder, Approaches for handling high-dimensional cluster expansions of ionic systems, npj Computational Materials **8**, 1 (2022), number: 1 Publisher: Nature Publishing Group.

[75] J. Reed and G. Ceder, Role of electronic structure in the susceptibility of metastable transition-metal oxide structures to transformation, Chemical Reviews **104**, 4513 (2004).

[76] K. Kang, D. Carlier, J. Reed, E. M. Arroyo, G. Ceder, L. Croguennec, and C. Delmas, Synthesis and electrochemical properties of layered $Li_{0.9}Ni_{0.45}Ti_{0.55}O_2$, Chemistry of Materials **15**, 4503 (2003).

[77] See Supplemental Material at for details on linear response analysis of $LiNiPO_4$; comparison between the computed U/J values for NiO across screening inversion schemes and VASP pseudopotentials; geometric self-consistency experiment for the linear response analysis of NiO; statistics on estimated oxidation states of selected transition metal species using the bond valence method; theoretical approach to examine the effect of on-site and inter-site corrections on forces in a simple one-dimensional bipartite Hubbard lattice. The Supplemental Material also contains Refs. [1, 5, 15, 48, 68, 87, 88].

[78] G. Moynihan, G. Teobaldi, and D. D. O'Regan, A self-consistent ground-state formulation of the first-principles Hubbard U parameter validated on one-electron self-interaction error, arXiv:1704.08076 [cond-mat] (2017), arXiv: 1704.08076.

[79] T. B. S. Jensen, N. B. Christensen, M. Kenzelmann, H. M. Rønnow, C. Niedermayer, N. H. Andersen, K. Lefmann, J. Schefer, M. v. Zimmermann, J. Li, J. L. Zarestky, and D. Vaknin, Field-induced magnetic phases and electric polarization in $LiNiPO_4$, Phys. Rev. B **79**, 092412 (2009).

[80] J. Perez-Mato, D. Orobengoa, E. Tasci, G. De la Flor Martin, and A. Kirov, Crystallography online: Bilbao crystallographic server, Bulgarian Chemical Communications **43**, 183 (2011).

[81] E. Fogh, O. Zaharko, J. Schefer, C. Niedermayer, S. Holm-Dahlin, M. K. Sørensen, A. B. Kristensen, N. H. Andersen, D. Vaknin, N. B. Christensen, and R. Toft-Petersen, Dzyaloshinskii-moriya interaction and the magnetic ground state in magnetoelectric $LiCoPO_4$, Phys. Rev. B **99**, 104421 (2019).

[82] P.-W. Ma and S. L. Dudarev, Constrained density functional for noncollinear magnetism, Phys. Rev. B **91**, 054420 (2015).

[83] S. K. Panda, B. Pal, S. Mandal, M. Gorgoi, S. Das, I. Sarkar, W. Drube, W. Sun, I. Di Marco, A. Lindblad, P. Thunström, A. Delin, O. Karis, Y. O. Kvashnin, M. van Schilfgaarde, O. Eriksson, and D. D. Sarma, High photon energy spectroscopy of nio: Experiment and theory, Phys. Rev. B **93**, 235138 (2016).

[84] H. Park, A. J. Millis, and C. A. Marianetti, Total energy calculations using DFT+DMFT: Computing the pressure phase diagram of the rare earth nickelates, Phys. Rev. B **89**, 245133 (2014).

[85] C. R. Harris, K. J. Millman, S. J. van der Walt, R. Gommers, P. Virtanen, D. Cournapeau, E. Wieser, J. Taylor, S. Berg, N. J. Smith, R. Kern, M. Picus, S. Hoyer, M. H. van Kerkwijk, M. Brett, A. Haldane, J. del Río, M. Wiebe, P. Peterson, P. Gérard-Marchant, K. Sheppard, T. Reddy, W. Weckesser, H. Abbasi, C. Gohlke, and T. E. Oliphant, Array programming with NumPy, Nature **585**, 357 (2020).

[86] B. Ochoa and S. Belongie, Covariance propagation for guided matching (2011).

[87] B. Silvi and A. Savin, Classification of chemical bonds based on topological analysis of electron localization functions, Nature **371**, 683 (1994).

[88] F. Hao, R. Armiento, and A. E. Mattsson, Using the electron localization function to correct for confinement physics in semi-local density functional theory, The Journal of Chemical Physics **140**, 18A536 (2014), publisher: American Institute of PhysicsAIP.